Morphotectonic and geodetic evidence for a constant slip-rate over the last 45 kyr along the Tabriz fault (Iran)

Magali Rizza, Philippe Vernant, J.F. Ritz, Michel Peyret, Hamid Reza Nankali, Amid Nazari, Yahya Djamour, Reza Salamati, Farokh Tavakoli, Jean Chery, et al.

Morphotectonic and geodetic evidence for a constant slip-rate over the last 45 kyr along the Tabriz fault (Iran)

Article *in* Geophysical Journal International · June 2013

DOI: 10.1093/gji/ggt041

CITATIONS
14

READS
213

12 authors, including:

Philippe Vernant
Université de Montpellier
107 PUBLICATIONS **3,436** CITATIONS
SEE PROFILE

Jean-François Ritz
Université de Montpellier
131 PUBLICATIONS **2,226** CITATIONS
SEE PROFILE

Shannon A Mahan
United States Geological Survey
127 PUBLICATIONS **1,153** CITATIONS
SEE PROFILE

Frédéric Masson
University of Strasbourg
161 PUBLICATIONS **2,614** CITATIONS
SEE PROFILE

Geophysical Journal International

Geophys. J. Int. (2013) **193,** 1083–1094
Advance Access publication 2013 March 08

doi: 10.1093/gji/ggt041

Morphotectonic and geodetic evidence for a constant slip-rate over the last 45 kyr along the Tabriz fault (Iran)

M. Rizza,[1] P. Vernant,[1] J. F. Ritz,[1] M. Peyret,[1] H. Nankali,[2] H. Nazari,[3] Y. Djamour,[4] R. Salamati,[3] F. Tavakoli,[2] J. Chéry,[1] S. A. Mahan[5] and F. Masson[6]

[1] *Géosciences Montpellier-UMR* 5243, *Université Montpellier* 2, 34095 *Montpellier, France. E-mail: LRizza@ntu.edu.sg*
[2] *National Cartographic Center (NCC), Meraj Av., Azadi Square, P.O. Box* 13185-1684, *Tehran, Iran*
[3] *Research Institute for Earth Sciences, Geological Survey of Iran, P.O. Box* 13185-1494, *Tehran, Iran*
[4] *Geomatics College, National Cartographic Center (NCC), Meraj Av., Azadi Square, P.O. Box* 13185-1684, *Tehran, Iran*
[5] *US Geological Survey, MS* 974, *Denver, CO* 80225, *USA*
[6] *Institut de Physique du Globe de Strasbourg*-UMR7516, *Université de Strasbourg/EOST, CNRS,* 67084 *Strasbourg, France*

Accepted 2013 January 29. Received 2013 January 21; in original form 2012 July 12

SUMMARY

Iran is an active continental domain accommodating the convergence between the Arabia and Eurasia plates. In northwestern Iran, deformation between the Central Iranian block and the Caucasus domain is mainly accommodated by right lateral strike-slip on the Tabriz fault. Cities and villages, including the city of Tabriz, have been destroyed by several strong historical earthquakes ($M \sim 7$). In this study, we compare the slip-rates estimated from geodetic measurements (radar interferometry and GPS) with those determined by dating a geomorphological offset of an alluvial fan along the Tabriz fault.

The GPS measurements along two profiles normal to the Tabriz fault suggest a slip-rate of $7.3 \pm 1.3\,\mathrm{mm\,yr^{-1}}$. The persistent scatterer radar interferometry analysis of Envisat satellite archives from 2003 to 2010 shows a velocity gradient ($6 \pm 3\,\mathrm{mm\,yr^{-1}}$) across the Tabriz fault in agreement with GPS results. Moreover, it reveals that most of the area located south of the Tabriz fault is affected by subsidence, and that some sections of the fault probably act as barriers to fluid migration which may have an impact on its mechanical behaviour. West of Tabriz morphotectonic investigations on an alluvial fan surface show a right-lateral cumulative offset of 320 ± 40 m. Luminescence analyses of the coarse matrix alluvial fan deposits provide an age of 46 ± 3 ka. This yields a slip-rate comprised between 6.5 and $7.3\,\mathrm{mm\,yr^{-1}}$ along this segment. These results suggest that the Late Quaternary slip-rate is in agreement with the present-day slip-rate estimated by geodetic measurements, showing no slip-rate changes during the past 45 000 yr. Short-term variations within the 45 000 yr related to temporal earthquake clustering over few seismic cycles cannot be ruled out, but if they exist, they do not affect the geodetic and the geomorphological estimates. This study is in agreement with previous ones suggesting that long-term slip-rates (i.e. averaged over several tens of seismic cycles) are consistent with geodetic estimated slip-rates (i.e. extrapolated from few years of interseismic observations), and suggests that perturbations of fault slip-rates are related to variations over few seismic cycles.

Key words: Seismic cycle; Radar interferometry; Palaeoseismology; Continental tectonics: strike-slip and transform; Dynamics: seismotectonics; Asia.

1 INTRODUCTION—TECTONIC SETTING

Iran is an active continental domain accommodating $\sim 22\,\mathrm{mm\,yr^{-1}}$ of the convergence between the Arabia and Eurasia plates (McClusky *et al.* 2003; Nilforoushan *et al.* 2003; Vernant *et al.* 2004). The deformation is accommodated by active faulting in the Zagros, Alborz and Kopet Dagh mountain belts and also in the eastern part of Iran (Vernant *et al.* 2004; Ritz *et al.* 2006). In the northwestern part of Iran, the N–S rate of shearing reaches about $14 \pm 2\,\mathrm{mm\,yr^{-1}}$ between the Central Iranian block and the Eurasian Plate. A significant part of this shortening is accommodated by strike-slip faulting south of the Lesser Caucasus (Karakhanian *et al.* 2004; Vernant *et al.* 2004; Masson *et al.* 2006; Djamour *et al.* 2011). Based on GPS measurements, a large part of the deformation in this region is concentrated along the right-lateral strike-slip Tabriz fault with a geodetic

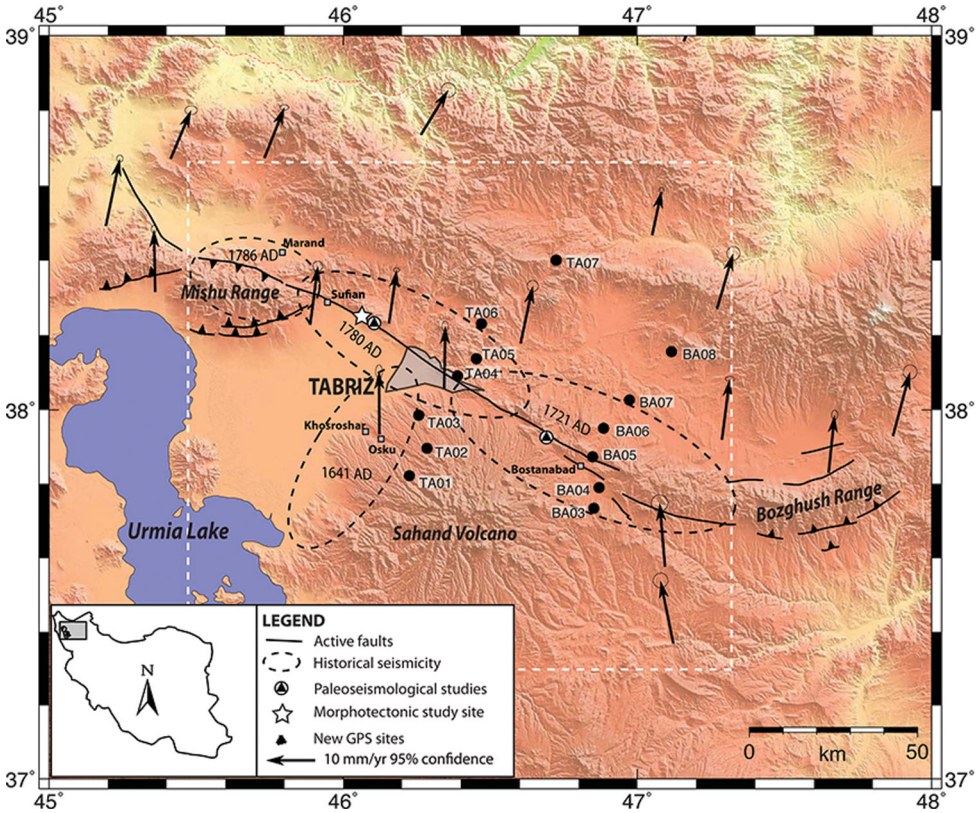

Figure 1. The Tabriz area and mapped active faults marked in solid black lines. The historical seismicity (isoseismics modified from Berberian & Yeats 1999) is represented by the dashed black ellipses, showing a propagation of rupture east to west over the time. The present-day GPS velocities from Djamour *et al.* (2011) are shown in Eurasia fixed reference frame with their 95 per cent confidence uncertainties. Previous palaeoseimological studies are located by the black triangles: trenches opened by Hessami *et al.* (2003) are west of Tabriz and results from Solaymani (2009) are east of Tabriz. The white star locates the morphotectonic study site close to Khadjeh-Marjan village. The white dashed box is for the areas shown in Figs 5 and 6.

slip-rate estimated at $\sim 7 \pm 1$ mm yr^{-1} (Djamour *et al.* 2011). Modeling of the geodynamics suggests that the Arabia–Eurasia convergence alone cannot explain this high slip-rate, and that a remnant subduction below the Caucasus or a delamination below the Lower Caucasus may still be active at present (Vernant & Chery 2006). The North Tabriz fault (NTF) trends NW–SE for more than 210 km and can be subdivided into several segments in a right stepping *en echelon* geometry (Berberian 1997; Karakhanian *et al.* 2004; Fig. 1). The fault cuts through Tabriz, one of the largest industrial cities of Iran with more than one million people. Microseismicity is associated with the Tabriz fault and most of the focal mechanisms show right-lateral strike-slip motion (Moradi *et al.* 2011).

Strong historical earthquakes have destroyed cities and many villages in Tabriz region and have inflicted heavy damage on Tabriz itself. The historical seismicity has been linked to the different segments of the Tabriz fault that seems to have ruptured during seismic clusters (Ambraseys & Melville 1982; Berberian & Yeats 1999; Hessami *et al.* 2003). The latest cluster occurred between 1721 A.D. and 1786 A.D. with three main earthquakes reported with magnitudes $M \sim 7$ (Fig. 1). In 1721 A.D., Tabriz was totally ruined by an earthquake ($M \sim 7.3$) with an epicentre on the eastern segment of the Tabriz fault (Berberian & Yeats 1999). In 1780 A.D. a destructive earthquake ($M \sim 7.4$) destroyed buildings in Tabriz and killed between 40 000 and 70 000 people (Berberian & Arshadi 1976). Berberian & Yeats (1999) placed the epicentre on the western Tabriz fault and mentioned that deep fissures, 2 m wide, had been reported in the area of the Sorkhab Mountain. After Berberian & Arshadi (1976), evidence for a recent surface rupture along the Khajeh-Marjan fault segment are clear and may be correlated with the historical 1780 A.D. earthquake. The 1786 A.D. earthquake ($M \sim 6.3$) occurred close to the city of Marand situated 60 km north of Tabriz. After Berberian & Yeats (1999), this event would be related to either the Mishu or the Sufian reverse faults located at the northwestern tip the Tabriz fault. In 1641 A.D. an earthquake ($M \sim 6.8$) destroyed Tabriz, as well as the Khosroshahr and Osku villages, with aftershocks felt for 6 months after the main shock (Berberian & Arshadi 1976). The epicentre for this earthquake was located south of Tabriz but does not correspond to any mapped fault (Berberian & Yeats 1999). Based on the historical seismicity, two other seismic clusters have been recorded between 1273 and 1304 A.D. and between 858 and 1042 A.D. in the region (Berberian & Arshadi 1976; Ambraseys & Melville 1982; Karakhanian *et al.* 2004). It is impossible to tell whether these two other clusters are associated with the Tabriz fault or if they were produced by other faults, given that the mezoseismal zones for these older earthquakes are not well-enough known. However, if we assume that these three historical seismic clusters were produced by the Tabriz fault, it yields a ~450 yr return period for seismic clustering along the Tabriz fault.

At Khajeh-Marjan (Fig. 1), a palaeoseismological study along the western Tabriz fault has shown that a minimum of four earthquakes, with coseismic offsets reported between 3 and 5 m, occurred during the past 3600 yr, with a mean estimated recurrence time of 821 ± 176 yr (Hessami *et al.* 2003). Another palaeoseismological study suggests that only three earthquakes occurred during the past 33 ka (Solaymani 2009). These results imply longer recurrence intervals

for earthquakes than the recurrence intervals estimated from the historical seismicity.

In terms of geological slip rate, morphological studies have estimated slip-rates ranging from 2 to 6.4 mm yr^{-1}, using offset stream incisions or other morphological markers, and assuming ages for alluvial deposits correlated with climatic records reported for the region (Pedrami & Anonymous 1987; Hossein-Khan-Nazer 1999; Hessami *et al.* 2003; Karakhanian *et al.* 2004). These estimates are lower than the present-day GPS-derived slip-rate along the Tabriz fault.

Therefore, the question remains as to whether slip-rate variations have occurred on the Tabriz fault during the Pleistocene–Holocene period. To help answer this question we propose to compare the slip-rates estimated from new geodetic measurements (GPS and radar interferometry) with those determined from a morphotectonic study in which we used optically stimulated luminescence to date an offset alluvial fan. In this study, we focus on the north-west segment of the Tabriz fault that ruptured during the historical 1780 A.D. earthquake.

2 GPS DATA PROCESSING AND VELOCITY FIELD

We used 13 new survey sites installed on two profiles across the NTF with an average spacing on the order of 10 km (Fig. 1). These new data fill the near field gap of GPS velocities of the Djamour *et al.* (2011) study. The western profile has seven sites and the eastern profile has six sites. All sites were surveyed at least 48 hr during each survey. The sites were surveyed four times during the fall of 2004, 2005, 2006 and 2008 except BA07 (2004, 2005 and 2006) and BA03 and TA04 (2005, 2006 and 2008). We use the GAMIT/GLOBK software package (Herring *et al.* 2009a,b,c) to compute the coordinates and velocities of the 13 survey GPS sites using a three-step strategy (Feigl *et al.* 1993; Dong *et al.* 1998). GPS data of 14 International GNSS Service (IGS) stations were introduced in the process to tie our local network to the ITRF reference frame. Our local quasi-observations were combined with the global quasi-observations provided by MIT (http://www-gpsg.mit.edu/~simon/gtgk/index.htm) from 1996 to 2009. According to Reilinger *et al.* (2006), we could account for the correlated errors in the time series by calculating a unique noise model for each continuous GPS station. Since our sites are only survey sites, we use the values determined by Djamour *et al.* (2011) for the Continuous GPS in NW Iran. In accordance with their study, we choose to use an equivalent random-walk noise of 0.95 mm yr$^{-1/2}$ to estimate the SGPS horizontal uncertainties. For the vertical random walk noise value we use 3 mm yr$^{-1/2}$. These values are consistent with those estimated by Djamour *et al.* (2011) for the Alborz Range. Finally, velocities and their 1σ confidence uncertainties were estimated in ITRF2008 and then the Eurasian reference frame was defined by minimizing the horizontal velocities of 23 IGS stations located in Europe and Central Asia as described in Djamour *et al.* (2011). The Weighted Root Mean Square (WMRS) value for the velocity residuals of these 23 sites is 0.1 mm yr^{-1}. The GPS velocities of our 13 SGPS sites and their uncertainties are given in a Eurasia-fixed reference frame (Table 1). Our data have been combined with the daily solutions of Djamour *et al.* (2011) to ensure the best combination. The velocity field is presented in the Central Iranian block-fixed reference frame in order to better illustrate the right lateral motion across the Tabriz fault (Fig. 2). The Central Iranian block-fixed reference frame has been defined using the Euler vector given by Djamour *et al.* (2011).

Table 1. East and north GPS velocity components (E Vel., N Vel.) and 1σ uncertainties (σE, σN) in a Eurasia-fixed reference frame as determined in this study are given in mm yr^{-1}. The correlation between E and N velocities (ρEN).

Lon. (°E)	Lat. (°N)	E Vel.	N Vel.	σE	σN	ρEN	Site
46.225	37.822	−0.55	13.36	0.61	0.63	−0.007	TA01
46.257	37.985	−0.72	12.89	0.63	0.65	−0.008	TA03
46.285	37.896	0.02	13.45	0.57	0.59	−0.004	TA02
46.389	38.091	0.88	12.59	0.69	0.72	−0.013	TA04
46.453	38.137	2.86	11.64	0.59	0.61	−0.007	TA05
46.470	38.231	4.16	10.82	0.63	0.65	−0.009	TA06
46.724	38.401	4.89	10.69	0.58	0.60	−0.012	TA07
46.848	37.873	1.02	12.31	0.59	0.61	−0.015	BA05
46.852	37.734	0.18	14.41	0.74	0.78	−0.003	BA03
46.870	37.790	−0.23	14.13	0.57	0.59	−0.005	BA04
46.885	37.950	2.29	14.36	0.58	0.60	−0.008	BA06
46.973	38.026	1.17	8.88	0.95	1.00	0.001	BA07
47.116	38.156	3.18	12.30	0.55	0.57	−0.006	BA08

As already pointed out by Djamour *et al.* (2011), the NTF is almost pure strike-slip fault and our profiles do not permit an improvement to their estimate of the fault-normal component (0–3 mm yr^{-1} of possible extension normal to the fault). For the fault-parallel component, we used the Savage & Burford (1973) model to fit the data of the two profiles and estimated a long-term geodetic slip-rate. This slip-rate is the upper bound value of the slip-rate since the main assumption of the model is that all the deformation is elastic and transient and will be reported on the fault during the earthquake. Fig. 3 presents the velocity component parallel to the fault and the fit to the data for the western and eastern profiles. Both agree on the right-lateral slip-rate estimates within the uncertainties (7.7 ± 0.9 and 7.2 ± 1.2 mm yr^{-1} for western and eastern profiles, respectively). The best estimated locking depth of 19 and 20 km depth (~±5 km) for the western and eastern profiles, respectively, are consistent with the depth of the microseismicity given by Moradi *et al.* (2011).

3 PSI ANALYSIS OF THE ENVISAT ARCHIVES

3.1 Methodology

In order to get a spatially dense image of the present-day ground deformation, we implemented a Radar Interferometry (InSAR) analysis of descending-track Envisat ASAR images that roughly span the same time interval as our GPS measurements (Fig. 4). Theoretically, InSAR is able to reach decametric resolution with subcentimetre precision in the measurement of surface displacements (e.g. Massonnet & Feigl 1998; Bürgmann *et al.* 2000). However, heavy geometrical and temporal decorrelation on the interferometric signal due to steep slopes on mountain belts, high vegetation coverage within valley, and variable weather conditions, seriously limit the efficiency of this approach (e.g. Zebker & Villasenor 1992; Zebker *et al.* 1997). The 'permanent-scatterers' (PS-InSAR) or 'persistent-scatterers' (PSI) radar interferometry techniques partly overcome these limitations (e.g. Ferretti *et al.* 1999, 2001). These methods consider the fact that, within spatially decorrelated areas, some pixels may exhibit some phase stability over a time-series of interferograms. For such pixels, called 'permanent' or 'persistent' scatterers (PS), one individual scatterer generally dominates the

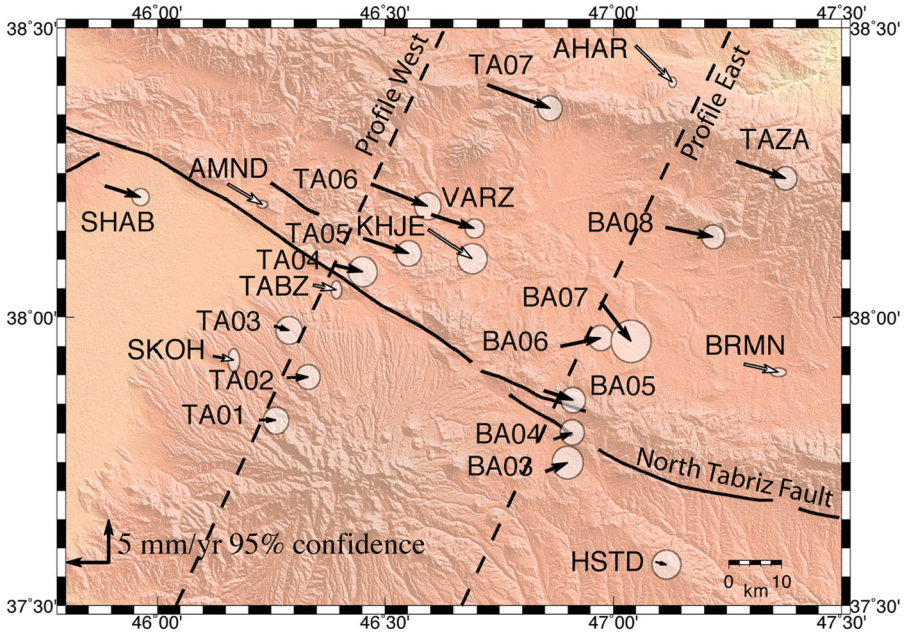

Figure 2. Map showing GPS velocities and 95 per cent confidence ellipses relative to the Central Iranian block. Black vectors are Survey GPS (SGPS) sites from this study (site names starting with BA0 and TA0) and from Djamour *et al.* (2011), white vectors are Continuous GPS (CGPS) sites from Djamour *et al.* (2011). The locations of the velocity profiles plotted in Fig. 3 are indicated by the black dashed lines.

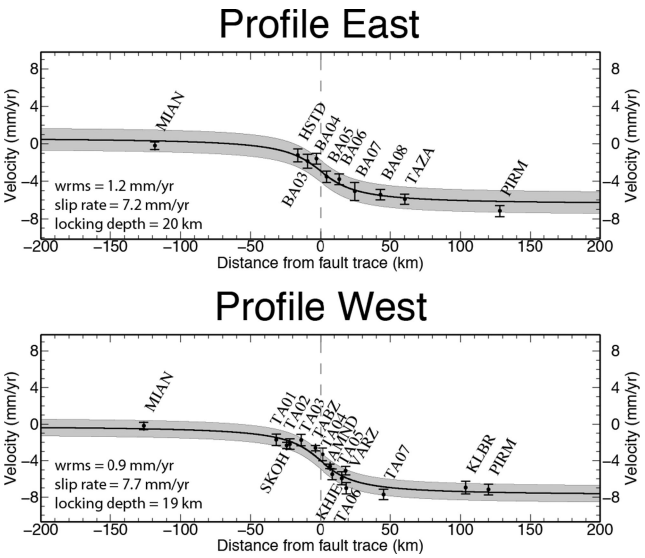

Figure 3. East and west fault parallel GPS velocity profiles (strike slip component) across the North Tabriz fault with 1σ uncertainties. The black curve shows the interseismic elastic deformation based on Savage & Burford (1973) model. The best-fitting parameters of this model (average fault slip rate, locking depth) are indicated as well as the Weighted Root Means Square (WRMS).

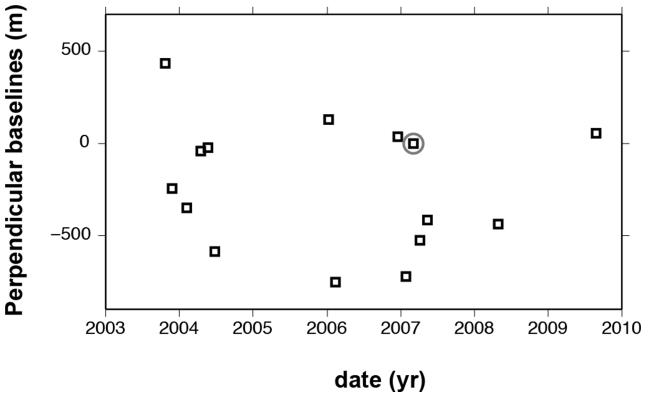

Figure 4. Set of Envisat radar images acquired in descending orbit processed in the PSI analysis. For each date of acquisition, this graph provides the perpendicular baseline relative to the master acquisition (2007 March 2, grey circle).

radar echo. Hence, PS pixels behave like point scatterers and decorrelation is greatly reduced. Moreover, over a set of interferograms, the phase signature of atmospheric delays (specific to each epoch), topographic artefacts (correlated with the perpendicular baseline) and continuous ground deformation can be discriminated (e.g. Ferretti *et al.* 2001; Kampes 2005; Hooper 2006). Based on this principle, several PS-InSAR approaches have been developed (e.g. Ferretti *et al.* 1999, 2001; Lyons & Sandwell 2003; Werner *et al.* 2003; Hooper *et al.* 2004; Kampes 2005). In this study, we use the 'StaMPS' (Stanford Method for Persistent Scatterers) method (Hooper *et al.* 2004, 2007; Hooper 2006). Contrary to most PS selection strategies, StaMPS uses spatial correlation of phase measurements to identify PS pixels (e.g. Hooper *et al.* 2004; Van der Kooij *et al.* 2005). For each candidate pixel, its probability of being a PS is estimated through phase analysis, which is successively refined in a series of iterations. This strategy allows the detection of PS pixels even where their amplitude is low, which is often the case in natural terrains, and without any prior assumption about the temporal nature of ground deformation. Instead of requiring a known temporal dependence of deformation, StaMPS simply relies on the spatially correlated nature of the deformation.

In this study, the differential interferograms have been constructed with 'Roi_pac' (Rosen *et al.* 2004) and 'Doris' software (Kampes *et al.* 2003). We used precise Envisat orbits from Delft (Kampes *et al.* 2003). We flattened and georeferenced the interferograms using the SRTM digital elevation model (Farr *et al.* 2007) that we oversampled to 1.5 s.

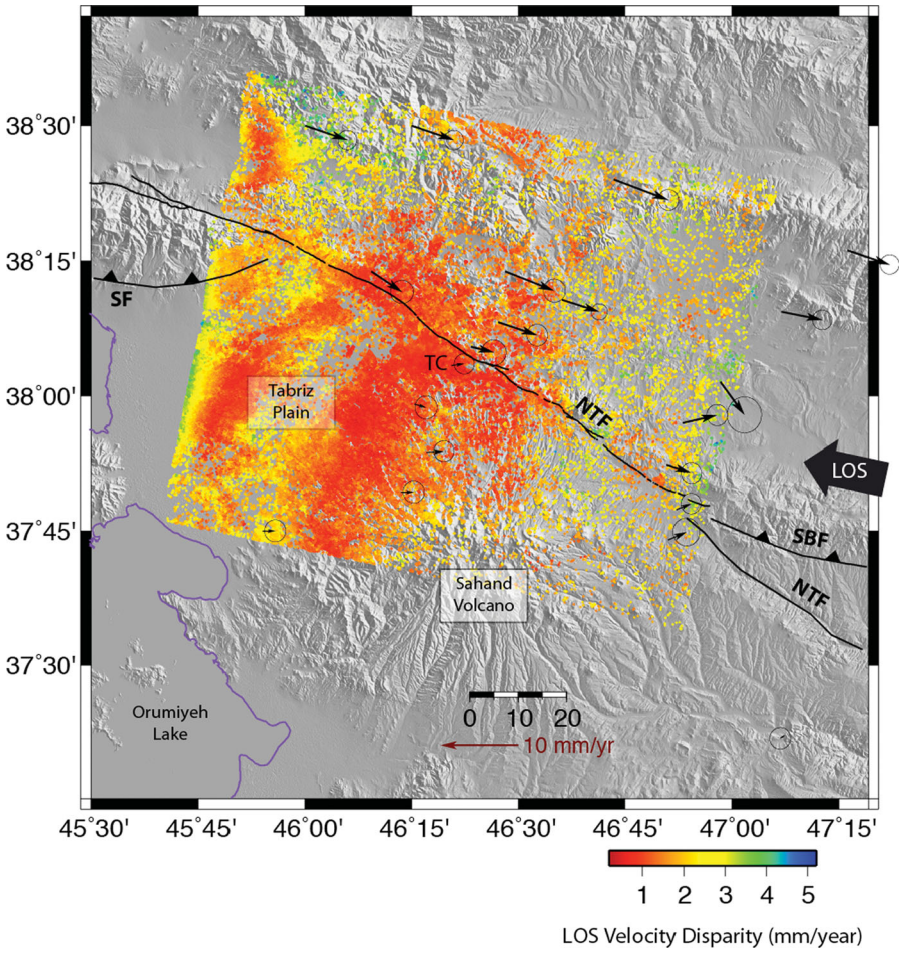

Figure 5. LOS velocity disparity relative to the mean PS velocity. This PS distribution has been obtained with a statistical threshold of 10 per cent of false PS. PS whose velocity disparity is higher than 2 mm yr^{-1} are further clipped to only retain the PS shown in Fig. 6. The GPS velocity field is relative to the Central Iranian Block with 95 per cent confidence ellipses. The thick black arrow on the right side of the figure indicates the satellite line of sight (LOS). SF, Sufian Fault; NTF, North Tabriz Fault; SBF, South Borzqush Fault; TC, Tabriz City.

3.2 Data set and processing parameters

Here we present the results of the PSI approach as applied to the Envisat satellite archives acquired on descending orbits between 2003 October and 2009 August, with a mean angle of incidence of 23° (Fig. 4). We chose this geometrical configuration because the satellite line of sight (LOS) is more collinear to the expected ground deformation than it would be in the ascending pass. Moreover, radar archives in ascending pass are too few for a reliable PSI analysis (only 4 and 10 images spanning only 4 yr in the two tracks that cover the study area). The PSI approach requires the selection of one master image with respect to which all other images are combined to form interferograms. We chose the acquisition of 2007 March 2 since it minimizes the global temporal and geometrical decorrelation in the formation of the interferograms time series. We processed the radar time-series with a wide range of thresholds related to the probability for a selected pixel to be a false PS (from 1 to 20 per cent). The higher the threshold, the higher the density of pixels selected as PS. However, the probability of including false PS will increase. Indeed, beyond a certain threshold (typically 10 per cent), we noted that in some areas the PS mean velocity field ceases to conform to the ones obtained with lower thresholds. Consequently, in order to avoid such discrepancy, we present in this study the PS mean velocity field that statistically includes no more than 10 per cent of false PS. Even with such a restrictive threshold, the spatial density of PS is fairly high. 195 000 PS have been selected over the whole scene. However their spatial density ranges from several tens, or even hundreds PS km^{-2} mainly in the Tabriz plain and the western flank of the Sahand volcano, to less than ∼10 PS km^{-2} elsewhere (Fig. 5). The standard deviation of the PS mean velocities (Fig. 5) is estimated to be less than 2 mm yr^{-1} over most of the study area. Nevertheless, a significant part of the scene exhibits higher standard deviations (up to ∼4 mm yr^{-1} in some places). For the mean velocity interpretation, with the aim of reliability, we remove PS whose disparity is higher than 2 mm yr^{-1}. Finally, we optimize (in a weighted least-square sense) the spatially linear transform that best fits the PS velocity field (in the vicinity of GPS sites) to the GPS velocity field projected along the satellite LOS. This allows us to convert the PS velocity field into the fixed Central Iranian block reference frame, while removing any possible orbital residuals. To be done rigorously, this would require knowledge of the vertical GPS velocities as well as the existence of any vertical component to the deformation. Morphological studies support a minor thrust component of the NTF (e.g. Karakhanian *et al.* 2004). However, as discussed below, most of the Tabriz plain, as well as probably a large part of the Sahand volcano, are affected by vertical deformation due to water withdrawal. Hence, the adjustment with GPS velocities has been performed without the SHAB

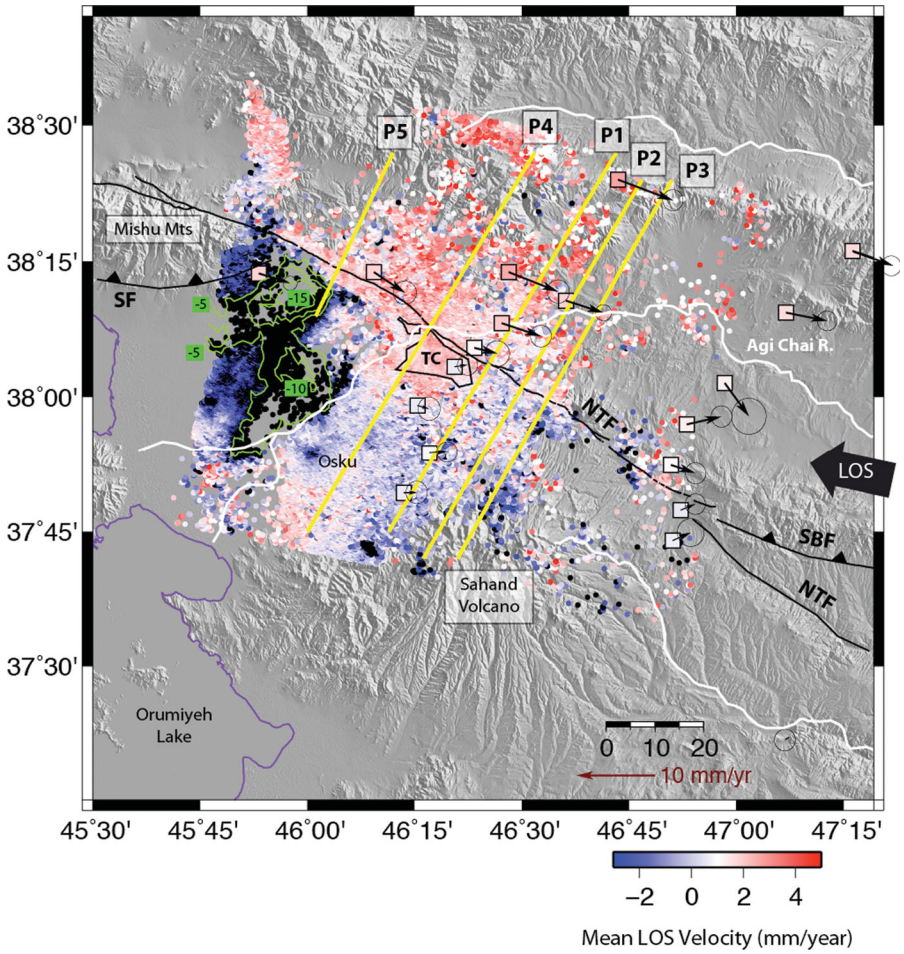

Figure 6. PS mean velocity map from Envisat archives in descending orbits. Black arrows and ellipses are the horizontal GPS velocity field relative to the Central Iranian Block with 95 per cent confidence ellipses. Coloured squares at GPS sites represent the GPS velocities projected onto the satellite LOS. The colour palette has been adjusted to the small tectonic velocity range expected in this area. Blue means away from the satellite, red means towards the satellite. Deformation largely exceeding this range is detected in the Tabriz Plain between the Agi-Chai River to the west and the North Tabriz fault to the north. In this case, only 5 mm yr^{-1} interval contours of the PS velocity are plotted. Profiles used in Fig. 7 are plotted with yellow lines. The thick black arrow on the right-hand side of the figure indicates the satellite line of sight (LOS). The limits of the Tabriz City and its airport are shown with black polygons. SF, Sufian Fault; NTF, North Tabriz Fault; SBF, South Borzqush Fault; TC, Tabriz City.

site, but may still have left a residual misfit that we estimate to no more than ∼1 mm yr^{-1} over the whole scene. The validity of this adjustment is confirmed *a posteriori* by the observation of null-gradient of PS velocities (within the PS velocity uncertainties) in the northern part of the scene where no detectable LOS deformation is expected. This adjustment led to the mean velocity map and profiles presented on Figs 6 and 7. For each GPS site, the horizontal GPS velocity vectors have been projected along the satellite LOS.

3.3 PS mean velocity field

The most salient pattern of deformation stands west of Tabriz and stretches over the part of the Tabriz plain bounded to the east by the Agi-Chai River, and to the north by the NTF. It is composed of two bean-shaped areas (∼300 km^2 each) that exhibit a continuous-in-time rate of deformation away from the satellite (Fig. 6). The peak velocity amplitudes are ∼10 and ∼15 mm yr^{-1} in their centres. These patterns of deformation are likely as a result of land subsidence induced by heavy water withdrawal for Tabriz tap water, as well as for agricultural and industrial purposes. In this industrial zone of Tabriz, one shallow and one deep aquifer are exploited, resulting in heavily polluted waste water (Baghvand *et al.* 2006). Even though one would normally expect seasonal variations or annual changes, the low temporal sampling of the radar acquisitions does not permit us to identify any significant temporal changes over the time interval spanned by the archives.

We used five profiles normal to the NTF to better illustrate the ground motion across the fault and to compare GPS velocities projected along the satellite LOS with the PSI results. PS velocities are collected within a 1-km-wide strip centred on the profiles displayed on Fig. 5.

The western GPS profile is located outside this major subsiding area (see location in Fig. 2). The profile P1 (Figs 6 and 7) follows this GPS transect, allowing for the comparison of GPS- and PS-velocity changes across the NTF. They agree quite well between distances of 20 and 60 km along the profile P1. Both indicate a gradual LOS-velocity change of 2 ± 1 mm yr^{-1}, most of which is accommodated over a distance of ∼30 km (between 25 km and 55 km along the profile). Due to the oblique geometry of the radar acquisition, there is an ambiguity in the ratio of vertical and horizontal velocities that produces 1–2 mm yr^{-1} LOS velocity. If we assume that all the displacement is horizontal, then 2 ± 1 mm yr^{-1} in LOS is equal

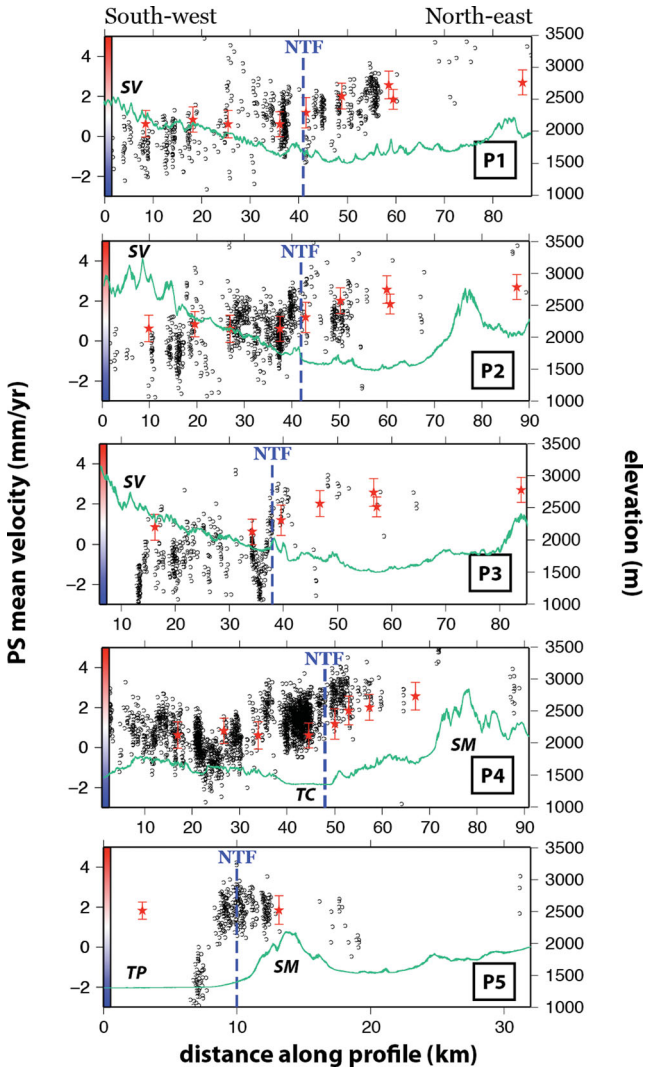

Figure 7. Comparison of GPS velocities along the satellite LOS and PS mean velocities for the five profiles whose locations are shown in Fig. 6. Colour palette on the left side is the same as for Fig. 6. The topographic profile is plotted in dark green. SV, Sahand Volcano; NTF, North Tabriz Fault; SM, Sorkhab Mountain; TC, Tabriz City; TP, Tabriz Plain.

to $6 \pm 3\,\mathrm{mm\,yr^{-1}}$ of fault parallel motion. Further north, the very low density of PS does not permit determination of any other additional deformation that occurs there. South of 20 km on P1, on the lowest slopes of the western and northern flanks of the Sahand Volcano, the PS-velocities are slightly lower than the GPS-velocities by $\sim 1\,\mathrm{mm\,yr^{-1}}$ LOS. Even though one may question the long wavelength adjustment of the PS velocity field, this latter pattern must certainly be related to the apparent global underestimation of the ground deformation by PS all over the Sahand Volcano (mean LOS velocity of $\sim -1\,\mathrm{mm\,yr^{-1}}$) where no significant horizontal deformation relative to the CIB is normally expected. In fact, the most important aquifer in the Tabriz surroundings is the alluvial tuff aquifer that stretches over the northern and western flanks of the volcano. Its mean groundwater level has steadily decreased from the years of 1985 to 2003 (Moghaddam & Najib 2006), and has probably kept on decreasing for the last decade, inducing the ground subsidence evidenced by the PS velocity field. Moreover, even high negative velocities ($\sim 5\,\mathrm{mm\,yr^{-1}}$) are even detected in some localized areas [i.e. close to the Osku Village (Fig. 6) and the Seghayesh Village at the southern extremity of the profile P1 in Fig. 7]. The negative velocities are probably related to water pumping for agricultural purposes in these narrow valleys. However, slow landslides could also explain some of these velocity patterns.

Approximately 10 km eastward from the western GPS transect, profile P2 suggests that an abrupt $\sim 1\,\mathrm{mm\,yr^{-1}}$ LOS velocity offset right across the NTF trace is now superimposed to a large scale velocity gradient similar to the one found on P1 but much noisier. The localized offset occurs over a distance of 4 km, between 38 and 42 km. As for profile P1, $\sim 1\,\mathrm{mm\,yr^{-1}}$ of additional LOS deformation (that we attributed to ground subsidence induced by water pumping) is mapped along the lower slopes of the Sahand Volcano (25 km and southwards).

The localized deformation on the NTF is even more conspicuous a few kilometres further east. Indeed, the profile P3 reveals a net discontinuity of ~ 2–$3\,\mathrm{mm\,yr^{-1}}$ LOS within just a few hundred meters across the NTF (38 km on P3). This velocity offset could be explained by a localized tectonic deformation due to a very shallow locking depth and/or a subsidence of the southern area related to water pumping. However, if one assumes that the locking depth of the NTF does not vary significantly along this section, then most of this localized deformation is very likely related to water pumping of the alluvial tuff aquifer bounded to the north by the NTF. This discontinuity of the PS velocity across the NTF probably persists further east. Unfortunately, the PS density drastically decreases eastwards, and no definitive conclusion can be drawn about the lateral extent of this discontinuity.

A profile west of Tabriz (profile P4), similarly to P1, reveals a gradual LOS velocity change of $\sim 2\,\mathrm{mm\,yr^{-1}}$ across the NTF (between 35 and 65 km). Subsidence probably occurs between 15 and 35 km, at the foot of the western flank of the volcano. However, the PS velocity field over Tabriz is $\sim 1\,\mathrm{mm\,yr^{-1}}$ LOS higher than we would expect from GPS. This suggests that this area is slightly uplifting, with the source being likely some local groundwater recharge.

Further west, the profile P5 shows that the limit of the subsiding zone is roughly parallel to the NTF, but located ~ 2 km south of it. No velocity discontinuity is observed across the NTF. This observation raises the question of the possible distribution of deformation over several subparallel faults in this section of the NTF (e.g. Karakhanian *et al.* 2004). As for the long-wavelength deformation, no conclusion can be drawn from this profile since the PS density is very low on the northern side of the fault, and the subsidence predominates in the deformation of the southern side. Finally, at the western end of our study zone, east of profile P5 up to the junction with the Sufian reverse fault, the NTF exactly coincides with the northern limit of the subsiding area (Fig. 6).

To summarize, our PS analysis has first revealed low ($\sim 1\,\mathrm{mm\,yr^{-1}}$ LOS) to high (~ 10–$15\,\mathrm{mm\,yr^{-1}}$ LOS) subsiding rates due to water pumping activities. This phenomenon is found in both the Tabriz plain and the northern and western flanks of the Sahand Volcano. Furthermore, a gradual LOS velocity offset of $2 \pm 1\,\mathrm{mm\,yr^{-1}}$ has been detected along the sections of the NTF that are not obscured by subsidence patterns. This is fairly consistent with the GPS measurements. Thus, assuming a pure right-lateral motion, the fault parallel motion is estimated to be $6 \pm 3\,\mathrm{mm\,yr^{-1}}$. East of Tabriz, a part of this gradient of deformation is accommodated within a very short distance which could suggest a shallow creep on this section of the fault and/or, more likely, a subsidence of a water table bounded to the north by the NTF. In this latter case, some parts of the NTF seem to act as barriers to fluid migration, which could have some implications on the local mechanical behaviour of the fault.

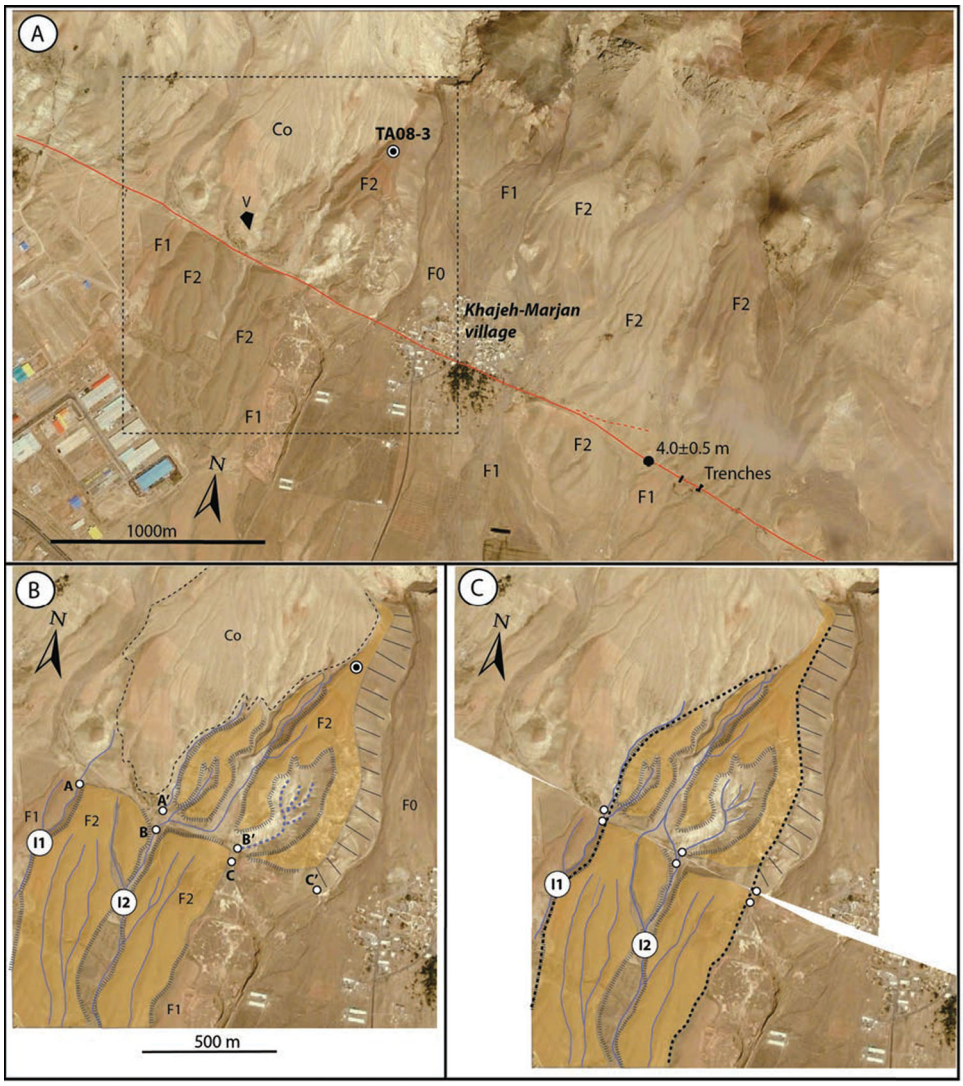

Figure 8. Google imagery and morphotectonic interpretations of the alluvial fan F2 displaced along the North Tabriz Fault (NTF), near the Khajeh-Marjan village (38.229°N, 46.095°E). (a) Google imagery of present day with general interpretations. The fault trace is in red, the dark dot represents the location for the smallest right-lateral offset measured in the field, also see Fig. 8. Trench locations are represented in the eastern part of the imagery (see also Hessami *et al.* 2003). TA08-3 is the luminescence sample collected within the coarse alluvial material. (V) is the point where field photography was taken in Fig. 9. The black dashed box represents the focus site in Fig. B. (b) Morphotectonic interpretations draped over the Google imagery for the present-day stage. The different piercing points (white dots) are AA′, BB′, CC′. (c) Morphotectonic interpretations draped over the Google imagery and reconstitution for an offset of ∼310 m. The black dashed lines represent the best reconstitution for the risers F2/F1. Note that for this reconstitution stream incisions are linked in both sides of the fault zone and piercing points are also well aligned.

4 MORPHOTECTONIC ANALYSES AND GEOLOGICAL SLIP-RATE

To estimate a geological slip-rate along the Tabriz fault, we focused our morphotectonic observations near the Khajeh-Marjan village, 2 km west of the palaeoseismological trenches of Hessami *et al.* (2003) (Figs 1 and 8a). In this area, large alluvial fans are observed and, using aerial imagery, we have identified three main surfaces of deposition.

4.1 Morphological observations

Our best observations were in the western part of the Khadjeh-Marjan village where an alluvial fan shows clear right-lateral cumulative offsets (Fig. 8). This alluvial fan surface (F2) contains a red varnish pavement that is covered by colluvial deposits (Co) in the northern part of the area (Fig. 8a). Deep incisions were observed within the F2 surface and are displayed as large cumulative offsets of several hundred meters along the Tabriz fault zone. South of the fault, the western riser of the F2 surface is bounded by a deep notch or channel (I_1), and a second incision can be identified in the central part of the fan surface (I_2, see Fig. 8b), which is now connected to streams north of the fault. Three piercing points A, B and C correspond to risers and major incisions (Fig. 8b).

North of the fault, several stream channels have been identified: west of the F2 surface a recent gash connects with the stream I_1, two deep notches connect with the I_2 stream valley, and a fourth stream channel of an abandoned valley (that does not cross the fault during modern times) can be identified (blue dotted line in Fig. 8b). In the field we have identified an abandoned stream channel, parallel to

Figure 9. Field view looking south of the incision stream I_2 right-laterally displaced along the fault zone with piercing point B–B′ (white dots). The white dashed lines highlight the stream channel.

the fault zone, showing that this incision was once connected to the I_2 valley (between B′ and B, Fig. 9). East of the alluvial F2 surface, an active stream has downcut into the riser between the F2 surface and the modern alluvium deposits (F0, Fig. 8b). Accordingly, we define piercing points A′, B′ to correspond to the deeper incisions within the F2 surface north of the NTF, and the piercing point C′ to correspond to the active stream in the youngest alluvial surface. Google Earth imagery (earth.google.com), aerial photography and Real Time Kinematic GPS survey have been used to estimate the offsets of the stream incisions. Our best reconstruction is presented in Fig. 8(c) where risers and stream incisions are well linked on both sides of the fault. We estimated offsets using the stream axis on both sides of the fault zone and using the risers between F2 fan surface and the thalweg incisions. We then calculated mean values for each piercing point with their associated uncertainties. The measured offsets are 343 ± 12, 311 ± 15 and 320 ± 40 m for the piercing points A–A′, B–B′ and C–C′, respectively. The weighted mean value for the stream offsets (A–A′ and B–B′) incising the F2 surface is 327 ± 30 m. Note that another study has estimated the offset of the alluvial fan at 500 m (Solaymani 2009). The difference of estimates can be explained by the distortion of the aerial photographs that we corrected using RTK GPS survey and orthorectified imagery.

In addition, after our field investigations, we estimated the smallest right-lateral displacement (an offset stream channel) to be 4 ± 0.5 m (Figs 8a and 10).

4.2 Luminescence dating and slip rate estimate

In order to date the F2 surface, one luminescence sample (TA08-3) was collected north of the fault zone (see location in Fig. 8a). To collect the luminescence sample, a soil pit was dug in the F2 fan deposits in which three main layers were identified (Fig. 11a). At the top of the pit, an organic-rich unit with a sandy matrix (∼10 cm thick) lies on a layer containing angular pebbles in a coarse sand matrix (∼35 cm thick). At the bottom, we observed a third unit containing angular pebbles, stratified and poorly sorted in a silty-sand matrix lies on a thin layer of red clay at ∼80 cm depth. The different sources for the angular pebbles are red sandstones and micaceous shales from the Palaeozoic formations and green-grey shales, sandstones and marly limestones from Mesozoic formations. The sample was taken within the clay layer at 80 cm depth using the collecting protocol detailed in Rizza *et al.* (2011). The fine material was preserved in a plastic bag inside an aluminum tube with both ends closed. We have also collected and sealed 600 g of coarse material for the dose rate estimation. The TA08-3 sample was prepared following the same protocol as Rizza *et al.* (2011). The cosmic doses and attenuation with depth were calculated using the methods of Prescott & Hutton (1994).

To analyse the quartz grains, we used the single aliquot regeneration (SAR) protocol (Murray & Wintle 2000, 2003) with the 250–180 μm quartz grains fraction, and a pre-heat temperature of 220 °C. Nineteen aliquots passed the test dose response and the equivalent doses ranged from 166 ± 13 to 238 ± 14 Gy, with a weighted mean equivalent dose estimated of 215 ± 14 Gy. The equivalent doses estimates are displayed on a radial plot following Galbraith *et al.* (1999) and also in a probability plot function (Fig. 11b). The ratio between the equivalent dose of TA08-3 and the dose rate (4.59 ± 0.1 Gy ka^{-1}) yields a burial age of 46 ± 3 ka for the F2 surface.

To analyse the feldspar component, we used the total-bleach Multiple-Aliquot Additive-Dose (MAAD) method for IRSL (Richardson *et al.* 1997; Aitken 1998; Forman & Pierson 2002) with the 105–90 μm grain size, after irradiation and a pre-heat of 124 °C for 64 hr. The equivalent dose for the sample is estimated at 242 ± 3 Gy and the dose rate at 6.17 ± 0.13 Gy ka^{-1}. Fading tests were carried out following the instructions of Auclair *et al.* (2003), and after a correction of 2.5 ± 0.5 per cent we obtain an age of 44 ± 1 ka using the formulas of Huntley & Lamothe (2001).

Using the offset with the larger uncertainty of 320 ± 40 m for the alluvial fan F2 and the ages from luminescence dating (46 ± 3 ka OSL and of 44 ± 1 ka IRSL), we estimate the

Figure 10. Field photograph of the smallest offset in the Khajeh-Marjan area (38.225°N; 46.106°E). White arrows represent the fault trace, white dashed lines show the stream channel boundaries and the white dots show the piercing points.

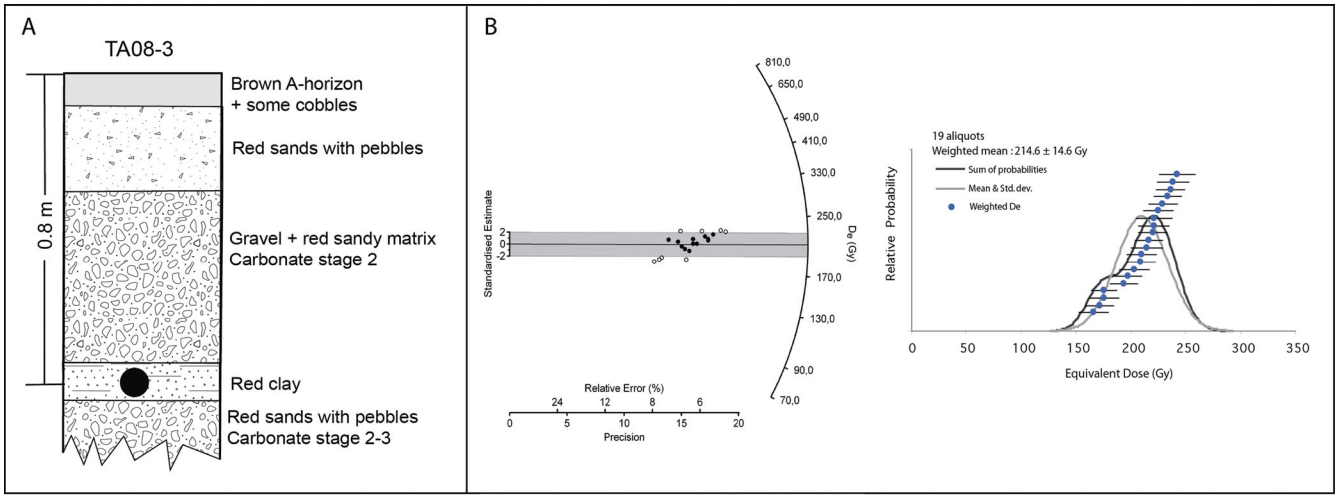

Figure 11. Soil pit stratigraphy where TA08-3 luminescence sample was collected within F2 alluvial surface. (a) The luminescence sample was collected in a red clay unit at 80 cm in depth (black dot). (b) Equivalent dose (De) distribution for TA08-OSL3 sample with the radial plot distribution at 2σ (95 per cent) following Galbraith *et al.* (1999) and the probability density plot (black line) with individual aliquots (blue dots) and the weighted age model distribution (grey line).

geological horizontal slip-rate for this segment to be between 6.5 and 7.3 mm yr^{-1}.

5 DISCUSSION—CONCLUSION

Using morphotectonic analyses, we have estimated a mean cumulative offset of 320 ± 40 m within an alluvial fan surface. Luminescence dating performed on the finer grained material within the alluvial fan yields an age between 43 and 49 ka. This age estimate is consistent with a period of siliclastic sedimentation, 45 km west of this study site, in the Orumiyeh lake area and may be correlated with the MIS 3 isotopic stage during a glacial period when the erosion and fluvial activities were intense (Djamali *et al.* 2008). Our Late Quaternary slip-rate lies between 6.5 and 7.3 mm yr^{-1} and is consistent with the 7.3 ± 1.3 and 6 ± 3 mm yr^{-1} deduced from the GPS observations and the PSI analysis, respectively. Although we cannot rule out temporal clustering on one or several

segments of the fault (e.g. Weldon *et al.* 2004). Our study shows that estimated geodetic slip-rates are consistent, within the uncertainties, with the estimated geological slip-rate over a long time period spanning several seismic cycles (e.g. Weldon *et al.* 2004; Reilinger *et al.* 2006, 2010). New morphotectonic studies need to be carried out along intermediate offset features to measure additional slip-rates.

Our estimate of the smallest right-lateral offset (4 ± 0.5 m) is consistent with previous estimates of coseismic offsets (3–5 m, Hessami *et al.* 2003; Karakhanian *et al.* 2004). Assuming that our measured offset corresponds to a characteristic slip for past earthquakes along this segment, and dividing it by the slip-rate (6.5–7.3 mm yr^{-1}) yields a recurrence interval comprised between 480 and 715 yr. This is consistent with the ∼450 yr time period separating seismic clusters reported in historical seismicity (Berberian & Yeats 1999). Our estimated recurrence interval is also concordant with the 821 ± 176 yr based on palaeoseismological investigations carried out at Khajeh-Marjan (Hessami *et al.* 2003).

Outside these seismic clusters, one strong earthquake in 1641 A.D. destroyed Tabriz (Ambraseys & Melville 1982; Berberian & Yeats 1999), but it is impossible to know from the historical data whether the Tabriz fault, or another nearby fault, was activated during this earthquake. This could be related to a chaotic seismic behaviour of the Tabriz fault with temporal earthquake clustering as evidenced for the San Andreas fault (e.g. Weldon *et al.* 2004) leading to short-term variations of the fault slip rate (averaged over a few seismic cycle). Only a complete palaeoseismological study could answer this question.

ACKNOWLEDGEMENTS

This work was completed within the framework of a co-operative research agreement between INSU-CNRS (DYETI, RNCC), MAE (French Foreign Office Ministry) and the National Cartographic Center (NCC, Tehran). We thank all the individual teams who went out in the field to collect the data, and those international colleagues who contributed data to the IGS Tracking network. All Envisat SAR data were provided and copyrighted by the European Space Agency. We are grateful to A. Hooper for the use of 'Stamps' software, and JPL/Caltech for use of the ROI_PAC software. We thank Richard Walker who drew our attention to the large-scale shifted fan feature at Khadjeh-Marjan, and Sharyar Solaymani, Hervé Philip and Stéphane Dominguez for fruitful discussions concerning the kinematics along the Tabriz fault. The interferometric processing was performed using the freely available Doris software package developed by the Delft Institute of Earth Observation and Space Systems (DEOS), Delft University of Technology. All figures were drawn using the Generic Mapping Tools (Wessel & Smith 1998). We also would like to thank the three anonymous reviewers and the editor, Prof. Duncan Agnew, for their constructive comments and their help to improve the manuscript.

REFERENCES

Aitken, M.J., 1998. *An Introduction to Optical Dating: The Dating of Quaternary Sediments by the Use of Photon-Stimulated Luminescence*. Oxford University Press.

Ambraseys, N.N. & Melville, C.P., 1982. *A History of Persian Earthquakes*. Cambridge University Press.

Auclair, M., Lamothe, M. & Huot, S., 2003. Measurement of anomalous fading for feldspar IRSL using SAR, *Radiat. Meas.,* **37,** 487–492.

Baghvand, A., Nabi, G.R., Mehrdadi, N., Givehchi, S. & Ardestani, M., 2006. Contamination of ground water in heavy metals concentration of Tabriz industrial zone, *J. appl. Sci.,* **6,** 1652–1658.

Berberian, M. & Arshadi, S., 1976. On the evidence of the youngest activity of the North Tabriz fault and the seismicity of Tabriz City, in *Contribution to the Seismotectonics of Iran, Part II,* pp. 397-418 ed. Berberian, M., Geol. Surv. Iran, Report 39, 397–418.

Berberian, M., 1997. Seismic sources of the Transcaucasian historical earthquakes, *Nato Adv. Sci. Inst. Ser., SER 2,* **28,** 233–311.

Berberian, M. & Yeats, R.S., 1999. Patterns of historical earthquake rupture in the Iranian Plateau, *Bull. seism. Soc. Am.,* **89,** 120–139.

Bürgmann, R., Rosen, P.A. & Fielding, E.J., 2000. Synthetic aperture radar interferometry to measure Earth's surface topography and its deformation, *Ann. Rev. Earth planet. Sci.,* **28,** 169–209.

Djamali, M. *et al.*, 2008. A late Pleistocene long pollen record from Lake Urmia, NW Iran, *Quat. Res.,* **69,** 413–420.

Djamour, Y., Vernant, P. & Nankali, H. *et al.*, 2011. NW Iran-eastern Turkey present-day kinematics: results from the Iranian permanent GPS network, *Earth planet. Sci. Lett.,* **307,** 27–34.

Dong, D., Herring, T.A. & King, R.W., 1998. Estimating regional deformation from a combination of space and terrestrial geodetic data, *J. Geodyn.,* **72,** 200–211.

Farr, T.G. *et al.*, 2007, The Shuttle Radar Topography Mission, *Rev. Geophys.,* **45,** RG2004, doi:10.1029/2005RG000183.

Feigl, K. *et al.*, 1993. Space geodetic measurement of crustal deformation in central and southern California, 1984–1992, *J. geophys. Res.* **98**(B12), doi: 10.1029/93JB02405.

Ferretti, A., Prati, C. & Rocca, F., 1999. Permanent scatterers in SAR interferometry, in *Proceedings of the International Geoscience and Remote Sensing Symposium,* Hamburg, Germany, pp. 1–3.

Ferretti, A., Prati, C. & Rocca, F., 2001. Permanent scatterers in SAR interferometry, *IEEE Trans. Geosci. Remote Sens.,* **39**(1), 8–20.

Forman, S.L. & Pierson, J., 2002. Late Pleistocene luminescence chronology of loess deposition in the Missouri and Mississippi River valleys, United States, *Palaeogeogr. Palaeoclimatol. Palaeoecol.,* **186,** 25–46.

Galbraith, R.F., Roberts, R.G., Laslett, G.M., Yoshida, H. & Olley, J.M., 1999. Optical dating of single and multiple grains of quatz from Jinmium rock shelter, Northern Australia. Part 1: experimental design and statistical models, *Archaeometry,* **41,** 339–364.

Herring, T.A., King, R.W. & McClusky, S.C., 2009a. *GAMIT Reference Manual, Release 10.3,* Massachusetts Institute of Technology, Cambridge, MA.

Herring, T.A., King, R.W. & McClusky, S.C., 2009b. *GLOBK Reference Manual, Release 10.3,* Massachusetts Institute of Technology, Cambridge, MA.

Herring, T.A., King, R.W. & McClusky, S.C., 2009c. *Introduction to GAMIT/GLOBK, Release 10.35,* Massachusetts Institute of Technology, Cambridge, MA.

Hessami, K., Pantosti, D., Tabassi, H., Shabanian, E., Abbassi, M., Feghhi, K. & Solaymani, S., 2003. Paleoearthquakes and slip rates of the North Tabriz Fault, NW Iran: preliminary results, *Ann. Geophys.,* **46**(5), 903–915.

Hooper, A., Zebker, H., Segall, P. & Kampes, B., 2004. A new method for measuring ground deformation on volcanoes and other natural terrains using InSAR persistent scatterers, *Geophys. Res. Lett.,* **31**(23), L23611, doi:10.1029/2004GL021737.

Hooper, A.J., 2006. Persistant scatterer radar interferometry for crustal deformation studies and modelling of volcanic deformation, *PhD thesis,* Stanford University.

Hooper, A., Segall, P. & Zebker, H., 2007. Persistent scatterers InSAR for crustal deformation analysis, with application to Volcan Alcedo, Galapagos, *J. geophys. Res.,* **112,** B07407, doi:10.1029/2006JB004763.

Hossein-Khan-Nazer, N., 1999. Geomorphological map of Sardrud, Geol. Surv. Iran Rep., sheet 5266 III, series K753.

Huntley, D.J. & Lamothe, M., 2001. Ubiquity of anomalous fading in K-feldspars and the measurement and correction for it in optical dating, *Can. J. Earth Sci.,* **38,** 1093–1106.

Kampes, B.M., Hanssen, R.F. & Perski, Z., 2003. Radar interferometry with public domain tools, *Paper presented at Third International Workshop on ERS SAR Interferometry, 'FRINGE03',* Frascati, Italy, 1–5 Dec 2003, p. 6.

Kampes, B.M., 2005. Displacement parameter estimation using permanent scatterer interferometry, *PhD thesis,* Delft University of Technology.

Karakhanian, A.S. *et al.*, 2004. Active faulting and natural hazards in Armenia, eastern Turkey and northwestern Iran, *Tectonophysics,* **380,** 189–219.

Lyons, S. & Sandwell, D., 2003, Fault creep along the southern San Andreas from interferometric synthetic aperture radar, permanent scatterers, and stacking, *J. geophys. Res.,* **108**(B1), 2047–2070.

Masson, F., Djamour, Y., van Gorp, S., Chery, J., Tatar, M., Tavakoli, F., Nankali, H. & Vernant, P., 2006. Extension in NW Iran driven by the motion of the south Caspian Basin, *Earth planet. Sci. Lett.,* **252,** 180–188.

Massonnet, D. & Feigl, K., 1998. Radar interferometry and its application to changes in the earth's surface, *Rev. Geophys.,* **36**(4), 441–500.

Moghaddam, A.A. & Najib, M.A., 2006. Hydrogeologic characteristics of the alluvial tuff aquifer of northern Sahand Mountain slopes, Tabriz, Iran, *Hydrogeol. J.,* **14,** 1319–1329.

Moradi, A.S., Hatzfeld, D. & Tatar, M., 2011. Microseismicity and seismotectonics of the North Tabriz fault (Iran), *Tectonophysics,* **506,** 22–30.

McClusky, S., Reilinger, R., Mahmoud, S., Ben Sari, D. & Tealeb, A., 2003. GPS constraints on Africa (Nubia) and Arabia plate motions, *Geophys. J. Int.,* **155,** 126–138.

Murray, A.S. & Wintle, A.G., 2000. Luminescence dating of quartz using an improved single-aliquot regenerative-dose protocol, *Radiat. Meas.,* **32,** 57–73.

Murray, A.S. & Wintle, A.G., 2003. The single aliquot regenerative dose protocol; potential for improvements in reliability, *Radiat. Meas.,* **37,** 377–381.

Nilforoushan, F. *et al.*, 2003. GPS network monitors the Arabia–Eurasia collision deformation in Iran, *J. Geod.,* **77,** 411–422.

Pedrami, M. & Anonymous, 1987. The absolute age of the base of the Olduvai Event is only 750,000 yr, *Congr. Int. Union Quat. Res.,* **12,** 240.

Pedrami, M., 1987. Quaternary stratigraphy of Iran, *Geol. Surv. Iran Rep.,* serial n. 551.79 (55) Pe [in Farsi].

Prescott, J.R. & Hutton, J.T., 1994. Cosmic-ray contributions to dose-rates for luminescence and ESR dating-large depths and long-term time variations, *Radiat. Meas.,* **23,** 497–500.

Reilinger, R. *et al.*, 2006. GPS constraints on continental deformation in the Africa-Arabia-Eurasia continental collision zone and implications for the dynamics of plate interactions, *J. geophys. Res.,* **111,** B05411; doi:10.1029/2005JB004051.

Reilinger, R. *et al.*, 2010. Geodetic constraints on the tectonic evolution of the Aegean region and strain accumulation along the Hellenic subduction zone, *Tectonophysics,* **488,** 22–30.

Richardson, C.A., McDonald, E.V. & Busacca, A.J., 1997. Luminescence dating of loess from the Northwest United States, *Quat. Sci. Rev.,* **16,** 403–415.

Ritz, J.F., Nazari, H., Ghassemi, A., Salamati, R., Shafei, A., Solaymani, S. & Vernant, P., 2006. Active transtension inside central Alborz; a new insight into northern Iran-southern Caspian geodynamics, Geology (Boulder), **34**(6) 477–480.

Rizza, M., Mahan, S., Ritz, J., Nazari, H., Hollinsgworth, J. & Salamati, R., 2011. Using luminescence dating of coarse matrix material to estimate fault slip-rate of the Astaneh Fault (Iran), *Quat. Geochronol.,* **6,** 390–406.

Rosen, P.A., Henley, S., Peltzer, G. & Simons, M., 2004. Updated repeat orbit interferometry package released, *EOS, Trans. Am. geophys. Un.,* **85**(5), 47.

Savage, J. & Burford, R., 1973. Geodetic determination of relative plate motion in Central California, *J. geophys. Res.,* **95,** 4873–4879.

Solaymani, S., 2009. Seismic hazard assessment for Tehran, Tabriz and Zandjan cities (NW Iran) based on morphotectonics and palaeoseismology, *PhD thesis,* University Montpellier 2, p. 150.

Van der Kooij, M., Hughes, W., Sato, S. & Poncos, V., 2005. Coherent target monitoring at high spatial density, examples of validation results, in *Proceedings of the Fringe 2005, ESA,* Frascati, Italy, November 28–December 2, 2005.

Vernant, P. & Chery, J., 2006. Low fault friction in Iran implies localized deformation for the Arabia–Eurasia collision zone, *Earth planet. Sci. Lett.,* **246,** 197–206.

Vernant, P. *et al.*, 2004. Present-day crustal deformation and plate kinematics in the Middle East constrained by GPS measurements in Iran and northern Oman, *Geophys. J. Int.,* **157,** 381–398.

Weldon, R.J., Scharer, K.M., Fumal, T.E. & Biasi, G., 2004. Wrightwood and the earthquake cycle; what a long recurrence record tells us about how faults work, *GSA Today,* **14**(9), 4–10.

Werner, C., Wegmüller, U., Strozzi, T. & Wiesmann, A., 2003. Interferometric point target analysis for deformation mapping, *Geosci. Remote Sens. Symp.,* IGARSS 2003. Vil. 7, pp. 4362–4364.

Wessel, P. & Smith, W.H.F., 1998. New, improved version of the Generic Mapping Tools released, *EOS Trans. AGU,* **79,** 579.

Zebker, H.A. & Villasenor, J., 1992. Decorrelation in interferometric radar surface echoes, *IEEE Trans. Geosci. Remote Sens.,* **30**(5), 950–959.

Zebker, H.A., Rosen, P. & Hensley, S., 1997. Atmospheric effects in interferometric synthetic aperture radar surface deformation and topographic maps, *J. geophys. Res.,* **102,** 7547–7563.